PNAS RESEARCH ARTICLE | APPLIED PHYSICAL SCIENCES OPEN ACCESS

Yardangs sculpted by erosion of heterogeneous material

Samuel Boury[a,1], Scott Weady[a,b,1], and Leif Ristroph[a,2]

Edited by David Weitz, Harvard University, Cambridge, MA; received December 19, 2023; accepted May 21, 2024

The recognizable shapes of landforms arise from processes such as erosion by wind or water currents. However, explaining the physical origin of natural structures is challenging due to the coupled evolution of complex flow fields and three-dimensional (3D) topographies. We investigate these issues in a laboratory setting inspired by yardangs, which are raised, elongate formations whose characteristic shape suggests erosion of heterogeneous material by directional flows. We combine experiments and simulations to test an origin hypothesis involving a harder or less erodible inclusion embedded in an outcropping of softer material. Optical scans of clay objects fixed within flowing water reveal a transformation from a featureless mound to a yardang-like form resembling a lion in repose. Phase-field simulations reproduce similar shape dynamics and show their dependence on the erodibility contrast and flow strength. Through visualizations of the flow fields and analysis of the local erosion rate, we identify effects associated with flow funneling and the turbulent wake that are responsible for carving the unique geometrical features. This highly 3D scouring process produces complex shapes from simple and commonplace starting conditions and is thus a candidate explanation for natural yardangs. The methods introduced here should be generally useful for geomorphological problems and especially those for which material heterogeneity is a primary factor.

geomorphology | flow-structure interaction | erosion | phase-field model

The shapes of landscapes and landforms give clues to the physical, environmental, and climatic conditions under which they formed (1–5). Such structures are typically complex, three-dimensional (3D), multiscale, and intricate. Similar morphologies are found in distant regions across the world—and indeed on other planets—suggesting that robust mechanisms underlie their formation. However, geomorphological interpretation is made challenging by many coupled complexities. For example, erosion by wind or water currents involves highly 3D flow fields that exhibit a vast range of length scales, from the generative scales of the atmosphere or ocean to millimetric boundary layers responsible for the removal of particulates. The associated time scales span those of the typically fast flows to the gradual shape development over eons. The flow fields and solid geometries evolve together in ways that are fundamentally interactive and interdependent (6, 7). Further, such flow-structure interaction problems typically involve temporal variability and spatial heterogeneity, for example, due to differences in material composition (8–12). In nature, all these complexities combine under uncertain conditions.

Some of these factors can be studied in laboratory experiments, models, and simulations that offer access to and control over the length and time scales (13–17). These approaches allow for manipulation and monitoring of the driving conditions as well as for direct observation and measurement of the resulting shape–flow coupled dynamics. The artificial setting of an experiment or simulation involves many of the aforementioned complexities, but under circumstances that permit detailed interrogation of parameters, testing of hypotheses, and identification of mechanisms. A consequence can also be the discovery of unexpected parallels between seemingly disparate systems. A case in point for erosion of noncohesive, granular materials is aeolian or wind-carved dunes in nature and similarly shaped aqueous or water-sculpted dunes in the lab (18–20). Such robustness may help explain why similar forms arise in different environments in nature. More generally, lab systems have proven useful for understanding other forms of shape-change processes such as weathering (21, 22), sublimation (23), dissolution (24, 25), and melting (26, 27).

Here, we combine lab experiments and simulations to understand shape–flow complexities and emergent formations in the case of cohesive solids subject to fluidic erosion. Our motivating context is a prevalent class of landforms called yardangs, which share some formative conditions with dunes but are composed of consolidated rock such as limestone or sandstone. These outcroppings of bedrock vary widely in size and can be found in isolation or in multitudes on Earth (3, 28–30) and elsewhere such as

Significance

This study addresses how the fluid mechanical erosion of a solid is affected by variability in its composition, which is important for understanding landforms, their shapes, development, and varieties. Our results reveal how variations in erodibility lead to intricate carving patterns due to changes in the surrounding flows that are responsible for removing material. We show specifically that such shape–flow feedback processes can sculpt structures that resemble yardangs, which are fascinating landforms shaped like lying lions and whose origin is not well understood. More generally, the experimental and computational methods developed here will be useful for other problems involving shape- and phase-change processes in geomorphology and applications for controlling erosion.

Author affiliations: [a]Department of Mathematics, Applied Mathematics Laboratory, Courant Institute of Mathematical Sciences, New York University, New York, NY 10012; and [b]Center for Computational Biology, Flatiron Institute, New York, NY 10010

Author contributions: S.B., S.W., and L.R. designed research; performed research; analyzed data; and wrote the paper.

The authors declare no competing interest.

This article is a PNAS Direct Submission.

[1] S.B. and S.W. contributed equally to this work.

[2] To whom correspondence may be addressed. Email: ristroph@cims.nyu.edu.

This article contains supporting information online at https://www.pnas.org/lookup/suppl/doi:10.1073/pnas.2322411121/-/DCSupplemental.

Mars (2, 28, 31). Yardangs are usually found in arid environments and predominantly shaped by wind erosion, though aqueous processes may also contribute (32–34). Subaqueous yardangs have also been documented (35), indicating that erosion by water currents can generate similar morphologies. The examples of Fig. 1 show why these formations are sometimes called mud lions, desert dogs, or sphinx-like yardangs. Their elongated form and prominent fore-aft asymmetry indicate carving by prevailing winds of a dominant direction (36–40), and the steeper windward side is documented to be harder and less erodible than the surrounding material (29, 33, 34, 41). Their development is thought to be driven by a combination of processes, predominantly abrasion by windborne particulates and deflation whereby loose material is removed by wind (36, 38, 42–45). The former depends on the impacting kinetic energy and the latter on the fluid shear stress, both of which are related to the flow speed near the solid surface (36, 46, 47).

Previous research aiming at explaining the shapes of yardangs has focused on global aspects and especially the elongated form of the base (32, 34, 42, 44). The more intricate characteristics evident in the examples of Fig. 1 are recognized as relating to material heterogeneity (30, 32, 38, 44, 48), but it remains unclear what conditions and local processes are responsible for generating the prow or head, its undercutting, and other features extending downwind along the base. Further, the existence of similar shapes in different environments—and indeed in air and water—suggests essential commonalities but which have not yet been identified. Related physics questions pertain to how material heterogeneity combines and interacts with other flow–structure complexities during the erosive reshaping of solids. To probe these issues, we conduct experiments on the erosion of clay by fast-flowing water and obtain highly resolved 3D measurements of the evolving geometry. This context also motivates the development of numerical simulations capable of solving for the coupled shape–flow dynamics in the challenging fluid dynamical regime characterized by boundary layers, flow separation, vortices, and turbulent wakes (49). To this end, we introduce a phase-field formulation that employs an empirically validated erosion model (14, 15) to numerically compute the flow field coupled to the solid topography and whose versatility helps to explore the key parameters at play in this process. We combine these approaches to test a minimal hypothesis for the formation of aqueous yardangs whose emergent features can be traced to shape–flow coupling effects.

Experimental Measurements of Shape Dynamics

We first test a minimal hypothesis for the formation of yardang-like structures through physical experiments involving erosion of a heterogeneous solid in flowing water. Our scenario considers a mound of erodible material containing an isolated hard, nonerodible inclusion. We propose that this idealized setting is emblematic of what may occur in nature when heterogeneities, formed perhaps in sedimentary layers of variable composition and compaction, are broken up and redistributed by processes such as local uplift and subsidence. The resulting material may be subject to flow with a prevailing direction and which we here idealize as uniform, unidirectional, and constant in the far field. Our realization in lab experiments involves a laminar flow water tunnel facility in whose test section bodies formed by bentonite clay are fixed and washed at high speed. The soft clay is built up around a cylindrical plastic inclusion and is shaped into an elongated hemiellipsoidal form. The clay is then placed on a flat platform which is mounted to a wall of the test section such that the major axis of the ellipsoid is aligned with the flow. The flow speed is controlled and stably maintained over the run time of several hours.

The chosen conditions and parameters are fully specified in *Materials and Methods*. The size scale of the body $L \sim 5$ cm and the flow speed $U \sim 50$ cm/s combine to yield a Reynolds number $\mathrm{Re} = \rho U L/\mu \sim 10^4$, where ρ and μ are the density and viscosity of the fluid (water). The high value of Re is associated with boundary layer flows on the windward surface of an object and turbulent and vortical wake flows shed downstream (49, 50). The clay is observed to erode with typical normal velocity $v_n \sim 1$ cm/h, yielding a large separation of timescales $U/v_n \sim 10^5$ indicative of slow shape evolution in the fast flow.

The 3D shapes and their evolution are complex, necessitating a technique capable of recording the geometry at high resolution. We opt for a structured light optical scanning method that projects patterns and captures many photographs as the object

Fig. 1. Examples of natural yardangs in isolation (*A*–*C*) and fields (*D*–*F*) from Egypt (*A*, *C*, *E*, and *F*), Argentina (*B*), and Namibia (*D*). Some common features include a raised "head" or prow that is typically undercut and which sits to one end of an elongated "body" or base extending along the ground. The formations of the *Top* row are approximately 15 m long and 10 m tall, and those of the *Bottom* row are approximately 5 m long and 2 m tall. Photograph credits: (*A*) K. Überschär; (*B*) K. Olmer; (*C*) E. Rovielo; (*D*) M. Welland; (*E*) J. Stephen; and (*F*) I. B. Cabral.

is slowly rotated on a stage, these data processed to yield a high-quality surface reconstruction (*Materials and Methods*). At regular intervals, we halt the flow, remove the platform from the tunnel, perform a scan over several minutes, and then return the structure to the tunnel and resume the flow. A representative sequence of shapes extracted every 30 min is shown in Fig. 2*A*. We also carry out control studies on mounds of homogeneous clay, as documented in Fig. 2*B* and which by comparison help to identify those features that can be attributed to the presence of the inclusion.

These experiments reveal a transformation from a featureless mound to a yardang-like form resembling a seated lion with a raised head. The events leading to this shape are closely tied to the inclusion, whose top is exposed by $t = 30$ min and from which slight gullies or channels can be seen extending downstream along what will become the lion's back. By 90 min, the hard head has been largely exposed by erosion around its sides and front, and the gullies have deepened. After 120 min strong undercutting of the inclusion is apparent, leaving the head connected to the body by a thinning neck. Ledges along the sides of the body are due to enhanced erosion downstream of the cheeks of the head. These processes continue through 150 min, by which time undercutting has left behind forelimbs and paws on the ground at the upstream base and erosion just behind the head contributes to the arched back. Soon after, the inclusion is completely excavated from the clay, at which time the experiment is stopped. The additional datasets provided in *Materials and Methods* show that these geometrical features and their temporal progression are reproduced with moderate variability between trials. Comparison to the case of Fig. 2*B* shows that the intricacies of the shape are caused by the inclusion.

Flow–Structure Interaction Simulations

To complement the lab experiments, we conduct three-dimensional numerical simulations (or "numerical experiments") of the flow–structure interaction problem. Here the equations of force and mass balance in the fluid are given by the incompressible Navier–Stokes equations

$$\rho\left(\frac{\partial \mathbf{u}}{\partial t} + (\mathbf{u}\cdot\nabla)\mathbf{u}\right) = \nabla\cdot\boldsymbol{\Sigma} + \mathbf{f}, \qquad [1]$$

$$\nabla\cdot\mathbf{u} = 0, \qquad [2]$$

where $\mathbf{u}$ is the fluid velocity, $\boldsymbol{\Sigma} = -p\mathbf{I} + \mu(\nabla\mathbf{u} + \nabla\mathbf{u}^T)$ is the stress tensor with p the pressure and μ the viscosity, and $\mathbf{f}$ is a body force. Previous studies have shown that the erosion rate of clay is proportional to the magnitude of the surface shear stress (14, 15). Explicitly, this results in a normal interface velocity of the form

$$v_n = -C|(\mathbf{I} - \hat{\mathbf{n}}\hat{\mathbf{n}})\cdot\boldsymbol{\Sigma}\cdot\hat{\mathbf{n}}| - m\kappa, \qquad [3]$$

where $\hat{\mathbf{n}}$ is the outward unit normal vector and $C(\mathbf{x})$ is the erodibility, which is viewed as constant in time but varying spatially within the heterogeneous material. The last term in Eq. **3** is proportional to the mean curvature κ and acts to smooth the boundary over a characteristic length determined by the parameter m. This is intended to suppress high curvatures that would induce numerical instabilities, and the term may also be interpreted as modeling additional erosive processes that preferentially act on sharp features. Defining $\boldsymbol{\Omega}(t)$ to be the solid domain and $\boldsymbol{\Omega}_i(t) \subset \boldsymbol{\Omega}(t)$ the inclusion domain, the erodibility is given by

$$C(\mathbf{x}) = \begin{cases} C_i & \mathbf{x}\in\Omega_i, \\ C_0 & \mathbf{x}\in\Omega\setminus\Omega_i, \end{cases} \qquad [4]$$

where C_0 is the erodibility of the clay and C_i the erodibility of the inclusion.

The framework described by Eqs. **1**–**4** can be solved using various methods; however, the complex and dynamic geometry poses challenges when explicitly representing the surface. Here, we use a phase-field formulation, which was originally developed for solidification and multiphase flows (51, 52) but has more recently been applied to moving boundary problems in contexts such as natural convective melting or dissolution (53–59). Similar models have been used to study erosion of soils under steady viscous flows (60–63), but to our knowledge have not yet been formulated and applied to erosion of heterogeneous materials coupled to unsteady or turbulent flows. In the phase-field model, the interface is implicitly represented by a continuous parameter

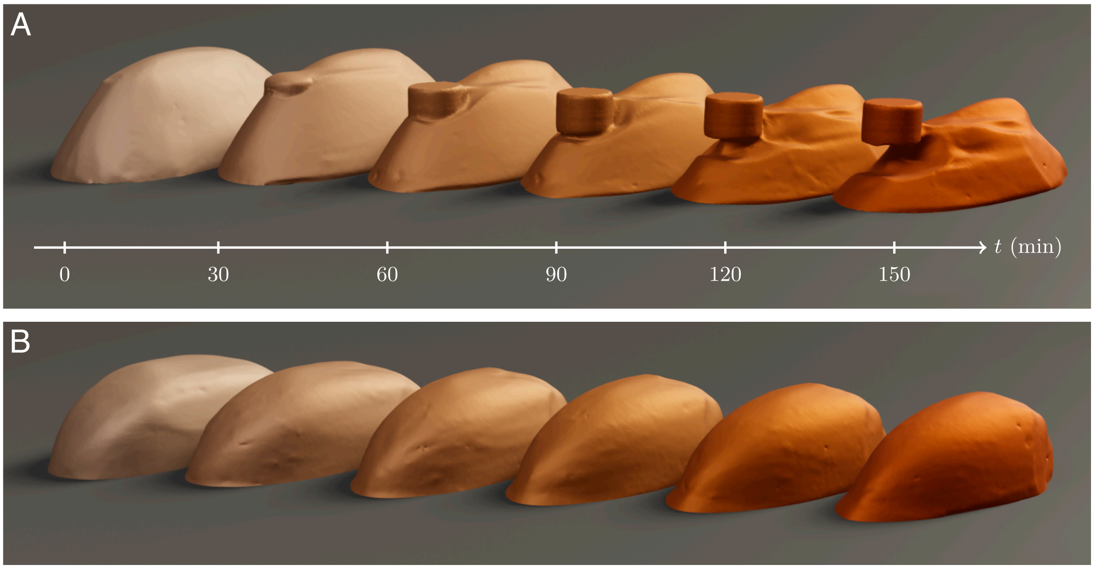

Fig. 2. Experimental measurements of the evolving shape of an erodible body subject to water current. A mound of soft clay with (*A*) and without (*B*) a hard inclusion is eroded within the flow of a water tunnel, and optical scanning records the shape every 30 min. The initial shapes are 12 cm × 6 cm × 4.5 cm in length, width, and height. The images display the extracted surfaces posed in a scene to show the progression in time. The presence of the nonerodible cylindrical inclusion, which becomes the head of the yardang-like structure, induces intricate features in the surrounding soft material.

$\phi(\mathbf{x}, t)$ such that $\phi = 0$ in the liquid domain and $\phi = 1$ in the solid, with the interface defined as the level set $\phi = 1/2$. Considering the trajectory of a point on the interface, it can be shown that the phase-field evolves according to

$$\frac{\partial \phi}{\partial t} = v_n |\nabla \phi|, \qquad [5]$$

where v_n is a field defined over all space via $\hat{\mathbf{n}} = -\nabla\phi/|\nabla\phi|$ and $\kappa = -\nabla \cdot (\nabla\phi/|\nabla\phi|)$. The solid is represented as a porous medium that exerts a drag force on the fluid of the form

$$\mathbf{f} = -\frac{\phi}{\eta}\mathbf{u}, \qquad [6]$$

where η characterizes the permeability, and $\eta \ll 1$ ensures negligibly small flow within the solid (64). Eqs. **5** and **6** can then be coupled to the fluid equations to simulate the moving boundary problem on a regular grid.

Our numerical implementation employs an approximate form of Eq. **3** that exploits the diffuseness of the interface. This extends Eq. **5**, which in principle is only defined on the interface, to the full computational domain. Specifically, the equation we solve is $\partial\phi/\partial t = -\tilde{C}|\nabla\phi \times \mathbf{u}|/\delta + m[\Delta\phi - \phi(1-\phi)(1-2\phi)/\delta^2]$, where δ is an interface thickness and $\tilde{C}$ is proportional to the erodibility C in Eq. **3**. (For simplicity, the tilde is omitted in what follows). Interpretations of this equation and related details on the numerical implementation can be found in *Materials and Methods*.

To mimic the experimental conditions, we consider flow in a three-dimensional rectangular channel with inlet velocity $\mathbf{u} = (U, 0, 0)$. The top and bottom walls are no-slip with $\mathbf{u} = \mathbf{0}$ at the bottom and $\mathbf{u} = (U, 0, 0)$ at the top, the sides are periodic, and at the outlet we set $\partial\mathbf{u}/\partial n = \mathbf{0}$ and $p = 0$. We initialize the body shape as a half-ellipsoid with principal axes $(4L, 2L, 3L)$, as shown in the leftmost image of Fig. 3. The simulation domain is taken to be twice the size of the body in each spatial dimension, which we find is sufficiently large for the boundary to have negligible effects on the shape dynamics.

Under these conditions, the system involves three key control parameters that can be cast as dimensionless groups of variables: the (initial) Reynolds number $\mathrm{Re} = \rho U L/\mu$, the clay erodibility $\gamma_0 = \rho U C_0$, and the inclusion erodibility $\gamma_i = \rho U C_i$. (Note that, as the body shrinks over time, the effective Reynolds number decreases.) The ratio of the latter two yields the relative erodibility $\sigma = \gamma_0/\gamma_i = C_0/C_i$, which characterizes the degree of heterogeneity of the material. Specifically, $\sigma = 1$ corresponds to a homogeneous material while the limit $\sigma \to \infty$ corresponds to a nonerodible inclusion, as pertains to the experiments.

Accurate solutions of the flow fields and solid geometry can be ensured for low to moderate Reynolds numbers, beyond which the computational costs become increasingly prohibitive. Fig. 3 shows snapshots of the evolving shape from a simulation at $\mathrm{Re} = 10^3$ and with $\gamma_0 = 5 \times 10^{-3}$, $\gamma_i = 5 \times 10^{-5}$ and thus $\sigma = 100$. The shapes correspond to the surfaces $\phi = 1/2$ at representative instants up to the final time t_f at which the material vanishes entirely. The shapes and their progression share some general aspects with those seen in experiments, albeit in muted form with softer features that might be expected given the lower Re. The strong fore-aft asymmetry due to the presence of the inclusion is apparent, as is the more subtle undercutting in the neck region and incision along the sides of the structure just downstream of the cheeks. The sides, back, and rear of the body are comparatively featureless, suggesting that the separated flows and wake are Re-dependent, as will be investigated further in subsequent sections.

While the effect of the relative erodibility σ is difficult to systematically investigate in experiments, the shape dependence on this parameter, as well as the Reynolds number, can be explored through simulations with relative ease. Fig. 4 presents morphologies across the space of (Re, σ) obtained through simulations starting from the same initial form. Each panel shows profile-view cross-sections of the body taken at equally spaced points in time up to the point where the homogeneous case has eroded to 50% its initial volume. The lowest row with $\sigma = 1$ represent control cases in which the solid is homogeneous. Several trends are apparent. Higher Re is associated with stronger fore-aft disparities in the erosion rates, and the overall shapes are more bulbous and less streamlined. The presence of the inclusion is clearly essential to giving the animal-like form with raised head, but for a given Re the characteristic shape differs little so long as $\sigma \gg 1$. For such high-σ cases, sufficiently high Re is needed to observe significant undercutting.

Experimental Flow Visualization

To better understand the underlying processes, we carry out flow visualization experiments using 3D-printed plastic models whose shapes are directly obtained from the surface scans of the eroding structures. We first use a coating method that distinguishes regions of attached and separated flows (65, 66). This technique consists of covering the model with a thin layer of a paste formed

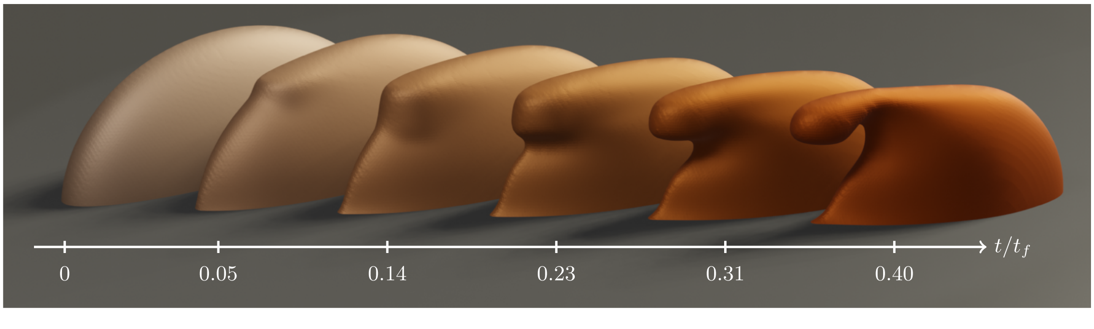

Fig. 3. Computed shape progression from phase-field simulations for the case of soft material with a hard inclusion. Several snapshots are displayed at different points of time, where t_f defines the time for the material to erode away entirely. The key parameters are the Reynolds number $\mathrm{Re} = 10^3$ and erodibility ratio $\sigma = 10^2$. The inclusion becomes the "head" that is excavated by erosion and especially undercutting in the "neck" region.

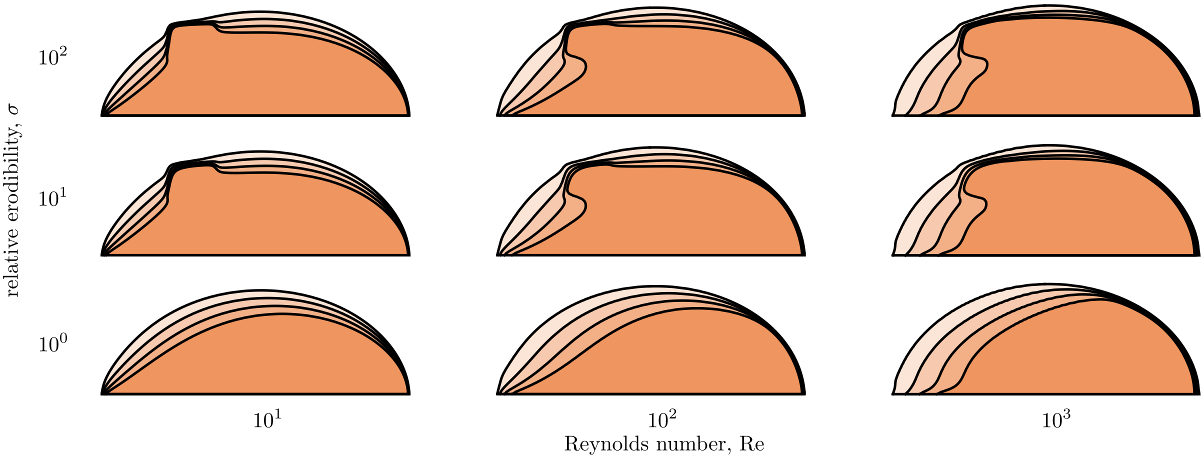

Fig. 4. Shape dependence on the Reynolds number Re and the relative erodibility σ obtained from the phase-field simulations. Each panel shows profile or cross-sectional views in the *xz*-plane at equal intervals up to the time where the homogeneous case ($\sigma = 1$, *Bottom* row) has eroded to 50% its initial volume at the given Re. Higher Re is associated with relatively stronger erosion at the front and thus a more prominent head.

by mixing clay powder with a concentrated solution of fluorescein dye, followed by imaging within the flow of the water tunnel. Complete details are available as *Materials and Methods*. Fig. 5 *A* and *B* present side- and overhead-view photographs, and Movies S1–S6 are also available. The colored region can be interpreted as the "streak volume," or set of all fluid parcels that have at some point come sufficiently close to the surface to pick up eroded material (49).

This method highlights the flows that separate from the structure and gives insights into the mechanisms operating in the associated regions. A strongly separated wake is seen just downstream of the inclusion, where vortex shedding gives the appearance of a billowing mane coming off the top and back of the head. This unsteady flow may be responsible for the locally higher erosion rate that gives rise to the arched back of the body. The very rear of the body is also in a fully separated wake flow, and its blunt, upright form is consistent with previous experiments on erosion of bluff bodies (14, 15). The sides are more nuanced, with attached flow near the front and separated flow near the rear. The sites of flow separation seem associated with abrupt changes in the shape, e.g. the concave region on the left side of the body in Fig. 5 *A* and *B* that has been hollowed out by the recirculating flow. The trials of Figs. 2 and 7 show considerable variability in these features, suggesting sensitivity to the details of the initial shape.

Aspects of the incoming stream and attached flows near the front are better revealed by the streakline visualization method (49, 66, 67), as shown in the photographs of Fig. 5 *C* and *D* and the associated videos. As described in detail in *Materials and Methods*, regularly spaced filaments of dye are released upstream of the 3D-printed model by feeding fluorescein solution through a manifold and out of thin tubes arranged in an array. Different planes are interrogated by orienting the model relative to the array.

The streaklines confirm that attached flows envelope the front of the structure, the face of the head as well as the neck, paws, and

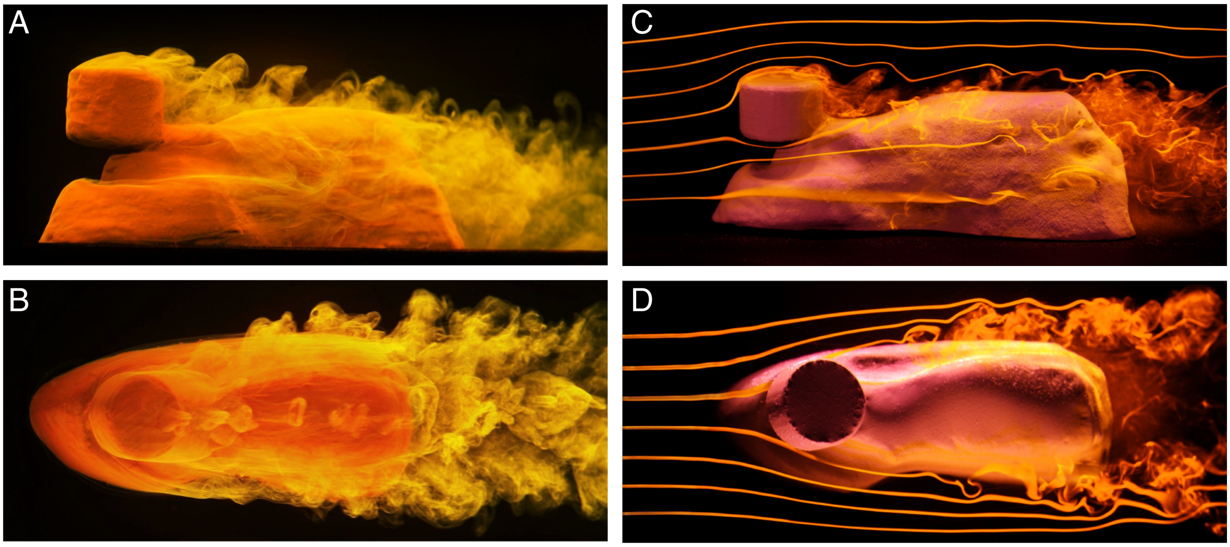

Fig. 5. Experimental flow visualizations around a model representing a late stage of the erosion process. The model is 3D-printed plastic whose form is obtained by an optical scan of the clay structure. (*A* and *B*) Side- and top-view visualizations via coating the model with a clay-dye paste. The images are photographs taken within the flow of the water tunnel, and the dyed material represents the "streak volume" of all fluid that passes sufficiently close to the structure. (*C* and *D*) Visualizations via dye filaments. The photographs capture streaklines of dye that are released upstream from an array of tubes (not shown).

shoulders, whereas separated flows occur over the top and back of the head, the back of the body, its rear, and leeward portions of the sides. The images reveal a particularly interesting flow impinging on the neck region just under the inclusion. In the vertical plane imaged in Fig. 5*C*, the streaklines are compressed as they turn downward under the chin of the head and upward over the paws. In the horizontal plane of Fig. 5*D*, a similar compression arises as the flow diverts around the front of the structure. These compounding effects indicate locally high flow speeds that could explain the rapid erosion that carves the neck and leaves the paws. In particular, since the flow in this region is observed to be steady, the streaklines correspond to streamlines whose relative spacing correlates inversely with flow speed via mass conservation of the incompressible fluid (49). In essence, a large area of the incoming flow is funneled into narrow streams that undercut the head and leave the ledges extending downstream along the body.

Phase-Field Analysis of Flow and Erosion Rate

The phase-field simulations provide further insights by connecting the flow fields to the local rate of erosion and its variations over the body surface. Fig. 6 *A* and *B* show side- and top-views of the streaklines (orange curves) from a later stage of a simulation with $\mathrm{Re} = 10^3$ and $\sigma = 100$. The general observations from experiments are confirmed, including the regions of attached and separated flows and, notably, the vertical and horizontal compression of the streaklines in the region below the inclusion. The coloring of the surface of the body corresponds to the local erosion rate, as indicated by the color bar. This information provides direct confirmation of the enhanced material removal rate in the neck region into which flow is funneled. One also observes locally high erosion rates in the wake of the head, though this effect is evidently insufficiently strong to yield appreciable arching of the back.

These simulations also quantify how the emergence of the inclusion affects local and global aspects of the erosion process. Fig. 6*C* assesses the total volume of the solid over time from simulations at $\mathrm{Re} = 10^3$, where the control case of a homogeneous body ($\sigma = 1$) is compared to the yardang-inspired case with a hard inclusion ($\sigma = 100$). The homogeneous material (orange curve) erodes in a manner consistent with a power law $V(t) = V_0(1 - t/t_f)^2$, as shown by the dashed curve. Here, V_0 is the initial volume and t_f is the time to vanish entirely. This form follows from previous scaling analyses based on boundary layer theory (14, 15, 68), and indeed the shape data of Fig. 4 for $(\mathrm{Re}, \sigma) = (10^3, 1)$ show that erosion occurs predominantly over the front surface where the flows are expected to be in stably attached boundary layers. The heterogeneous body (dark brown curve) initially follows the same law, then deviates due to slower overall erosion rate, and later tends to return to the predicted form. The intermediate stage corresponds to the period after the inclusion has been exposed (first dashed vertical line) and before the neck pinches off and the head detaches from the body (second line).

Although the global erosion rate slows due to the hard head, the local rates of the nearby softer material increase considerably. Fig. 6*D* shows the maximal erosion rate over the surface as a function of time for the same simulation run. Following a brief transient during which the flow field develops, the peak rate is seen to steadily increase over time for the yardang case, overtaking the control case and eventually reaching almost twice as strong erosion. Throughout the phase in which the head is exposed, this enhanced erosion consistently occurs in the region just below the inclusion. Later after the neck pinches and the head detaches, the maximal rate closely follows the control case.

Conclusions and Discussion

This experimental and computational study addresses how fluid mechanical erosion of a solid is affected by spatial variations in its composition. The main phenomenon uncovered here is a highly three-dimensional form of hydrodynamic scouring (69–71) in which regions of hard or weakly erodible material are excavated due to locally enhanced erosion of the surrounding softer material. This enhancement is driven by changes in

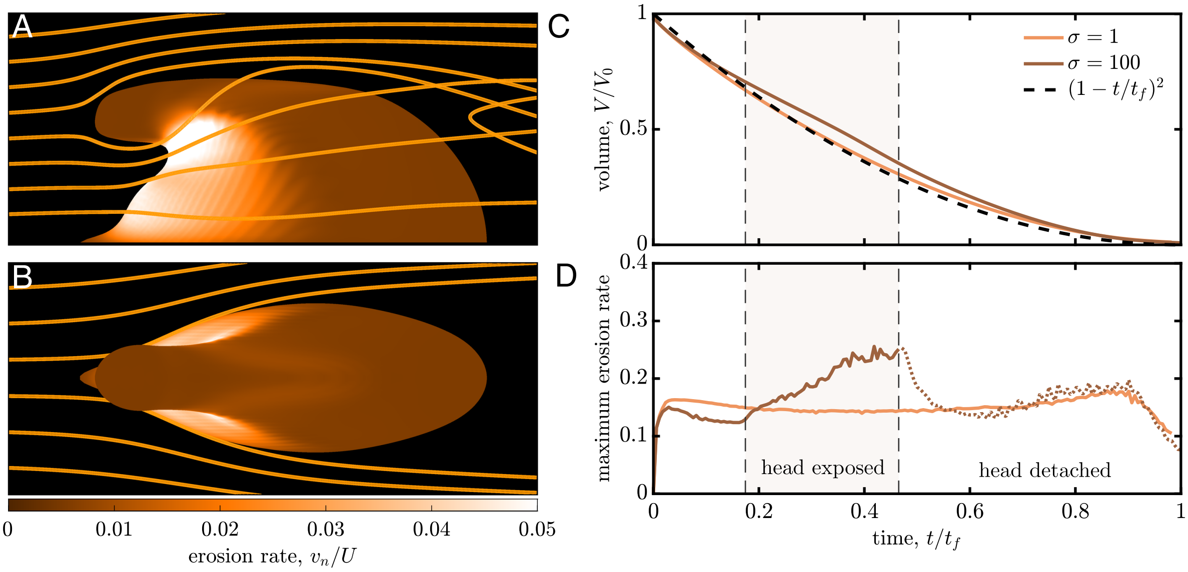

Fig. 6. Analysis of flow and erosion rate in simulations. (*A* and *B*) Streaklines (orange curves) and local erosion rate v_n/U (color map) at a late stage and for $\mathrm{Re} = 10^3$ and $\sigma = 100$. The highest erosion rates are induced near the inclusion. (*C*) Volume of the solid over time with ($\sigma = 100$, dark brown curve) and without ($\sigma = 1$, orange) the inclusion. The latter case follows a power law (dashed curve). (*D*) Maximal erosion rate on the surface versus time. During the phase in which the head is exposed and still attached, the maximal erosion rate overtakes the control case.

the flow field that occur when a hard inclusion is exposed, acting as an obstacle around which the incoming flow must accelerate and inducing an unsteady wake downstream. These effects are shown to lead to yardang-like formations for isolated inclusions embedded in hillocks of softer material subject to uniform incoming flow. More generally, our findings show how intricate 3D morphologies can emerge from relatively simple initial conditions due to complex shape–flow interactions.

The sculptures in our laboratory and computational systems resemble one another, but the formative conditions and processes involved differ in several respects. In simulations, we impose a simple law in which the local erosion rate varies in proportion to the surface shear stress (14, 15). A linear erosion-stress relationship has been shown to apply to the clay-water system for sufficiently high shear rates, and a more complete description may involve a yield stress, other nonlinearities, and time-dependent behavior due to water absorption. The range of Reynolds numbers $\mathrm{Re} \leq 10^3$ in our computational system is limited and spans what is considered the intermediate regime for external flows. Our experiments, on the other hand, operate at $\mathrm{Re} \sim 10^4$, yielding finer flow features and consequently more intricate etchings on the surface.

Natural yardangs form under more complex conditions involving temporally fluctuating flows that vary spatially within the atmospheric boundary layer. Moreover, the Reynolds numbers in such conditions are expected to be orders of magnitude larger than those considered here. The relevant aeolian processes depend not only on the wind field, but also on airborne particulates whose concentration and kinetic energy also vary in space and time (36, 38, 42–45). What the different systems seem to have in common is an erodible solid of heterogeneous composition (9, 12, 33, 34, 38, 41, 72), fast flow of a dominant direction (36–39), and local coupling between the two in which erosion depends on shear stress (14, 15, 36, 46, 47) and is influenced by vortex shedding, turbulence, and return flows (33, 34, 40). These are perhaps minimal ingredients for the formation of such structures.

Interestingly, it has been hypothesized that Egypt's Great Sphinx represents a modification of what was once a natural formation (73–75). The resemblance to actual yardangs and our laboratory and computational analogues is intriguing. Geological studies indicate that the core structure is indeed in situ rock of heterogeneous composition (76), but archaeological surveys suggest that the excavation of the body was largely or entirely anthropogenic. Our findings add little to this discussion, except perhaps to offer some general insight into the prevalence of animal-shaped landforms that could have inspired this monument.

Our study introduces methods that may be valuable for investigating other geomorphological problems. Experimentally, the clay-water system could be useful for understanding the erosion of cohesive solids, the fluid mechanics of which is far less studied than that of granular materials. The conditions of the laboratory setting can be tuned and the space- and time-scales adjusted such that the shape dynamics are tractable, as demonstrated here by 3D scanning at regular intervals. Subtle mechanisms can be inferred from the flow fields and their spatiotemporal complexities, as interrogated here through streak volume and streakline visualizations. Computationally, the phase-field formulation is a powerful and versatile means for numerically simulating shape–flow coevolution problems. It readily accommodates a wide range of flow conditions, complex solid geometries of variable composition, and different erosion physics as modeled by a boundary evolution law. These capabilities are particularly well suited for studying the diverse class of formations for which material heterogeneity and/or 3D flows are thought to be important (77–79).

Materials and Methods

Erosion Experiments. Soft clay is prepared by blending bentonite nanoclay powder with water in a 1:2 mixture by weight. The clay is pasted onto an acrylic plastic platform that can be mounted flush to the lid of the test section of a laminar flow recirculating water tunnel (Engineering Laboratory Design, Inc.). The clay is shaped into a half-ellipsoidal structure measuring 6 cm × 4.5 cm × 12 cm in width, height, and length. The long axis is to be aligned with the flow. Control experiments without an inclusion involve homogeneous mounds of clay. Yardang experiments with a nonerodible inclusion involve building up clay around a short upright cylinder of hard plastic that is secured to the platform via a thin, rigid stem. The cylinder is somewhat elevated off the platform and near the front of the mound. It has height 1.5 cm and diameter 2 cm, and its center location is 5 cm in front and 2.25 cm above the center of the ellipsoid's base. The prepared clay structures are eroded within the tunnel's test section measuring 15 cm × 15 cm × 43 cm in width, height, and length. The chosen flow speed of $U = 45$ cm/s yields a convenient run time of several hours. The resulting Reynolds number based on the half body width is $\mathrm{Re} \sim 10^4$. Tests at half and twice the speed yield similar shape evolution. Trials at yet lower speeds are contaminated by significant water absorption by the clay (14, 15), and yet higher speeds are not accessible in the water tunnel.

The 3D shape of the clay object is recorded at regular intervals via a structured light optical scanner (Shining 3D EinScan). The flow is stopped every 30 min, and the platform is removed and placed on the rotating bed of the scanner, which projects light patterns and records images that are postprocessed into a surface geometry file. The quality is enhanced by dabbing the platform dry to prevent reflections and inclining the lid and clay object such that the neck and chin region is well imaged. The platform is then returned to the tunnel and the flow restarted. The procedure yields seven scans in 3 h, by which time the neck typically erodes through and exposes the stem supporting the head. Fig. 2 *A* and *B* show representative datasets corresponding to the first six scans for cases with and without an inclusion, respectively.

Repeated trials are conducted to assess the consistency of the results. The scans of Fig. 7 *A*–*C* represent three additional runs for the same basic conditions as in Fig. 2*A* but with slightly different initial forms due to the manual shaping procedure.

Flow Visualization Experiments. The flows are visualized around high-fidelity plastic models of the clay structure at a late stage when it has developed into the yardang-like form. The surface geometry file obtained by scanning is converted to a solid geometry file and sent to a stereolithographic resin 3D printer (Formlabs Inc., Form 3L). One set of experiments serves to visualize the erosion process and the wake flows. The model is uniformly coated with a thin layer of a paste formed by blending clay powder with a concentrated solution of fluorescein dye in a 3:1 ratio. The model is placed in the flow of the tunnel and photographed with a digital camera (Nikon D610) under the illumination of several bright lamps. High contrast is provided by matte black paneling placed inside the tunnel walls, and the images are captured before the polluted fluid in the recirculating system returns to the test section. The side and overhead views of Fig. 5 *A* and *B* are obtained by affixing the structure to the floor and side wall of the tunnel, respectively. Global corrections applied to the images include recoloring and enhancing brightness and contrast. To avoid excessive dispersion of the dye, these experiments are conducted at a slower flow speed of 11 cm/s on an at-scale model, yielding a Reynolds number that is one-quarter of the value for the erosion experiments.

A second set of visualization experiments produced the streakline images of Fig. 5 *C* and *D*. A schematic of the setup is given in Fig. 8*A*, where the particular arrangement shown yields an overhead-view photograph. The 3D-printed model is again mounted in the tunnel on black background paneling and under appropriate lighting where it is imaged by a camera. Upstream is an array of hypodermic tubing from which dye is fed into the flow. A detailed view

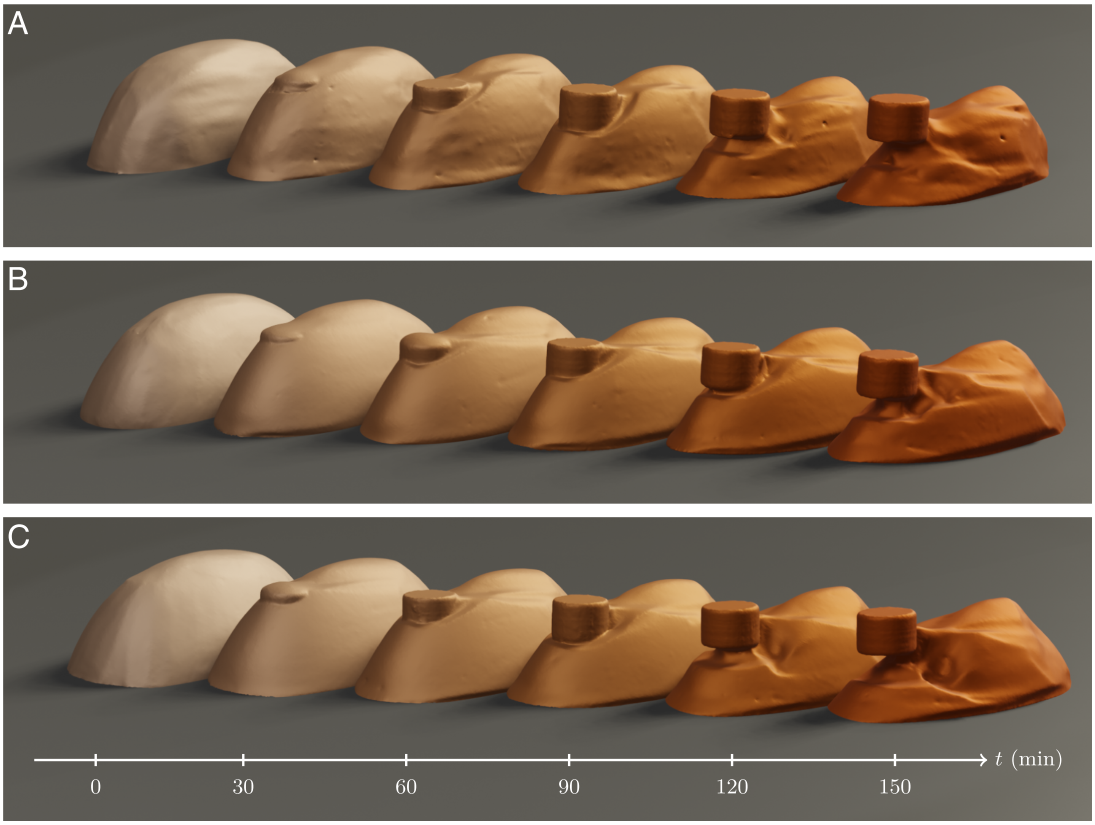

Fig. 7. Reproducibility of erosion experiments. (*A*–*C*) Shape progression from three representative trials. The initial shapes are 12 cm × 6 cm × 4.5 cm in length, width, and height. Comparison to Fig. 2*A* shows that general features of the shapes are reproduced while the sides of the structures display significant variations.

of the custom-made array system is shown in Fig. 8*B*. The dye is a concentrated fluorescein solution that drains via gravity from a container (not shown). For this purpose, we employ a Mariotte bottle that ensures constant flow rate. The hypodermics have inner and outer diameters of 0.61 mm and 0.76 mm, and they are spaced by 1 cm. To minimize flow disturbances in the plane of visualization, the hypodermics are bundled into a foil-shaped fairing, and their extremities are bent away from the fairing and into alignment with the flow. The fairing enters the test section through a slotted hole in the top wall, and the desired plane is achieved by sliding the support along positioning rails. The overhead view of Fig. 5*C* is achieved as shown in Fig. 8*A*, and the side view of Fig. 5*D* involves mounting the structure on the floor of the tunnel and translating the dye array accordingly.

Straight rather than sinuous filaments were achievable only at lower tunnel speeds. Hence, the streakline experiments are conducted at 11 cm/s on a model scaled up by 2, yielding a Reynolds number that is one-half of the erosion experiments. Other factors played a role in the quality of the filaments. The bends in the hypodermics should be of gentle curvature (here, ∼1 cm radius), and the openings of the tubes must be meticulously deburred and chamfered. It is helpful but not necessary to match the dye feed rate to the tunnel flow speed, the former adjusted here through the height of the Mariotte bottle. Matching

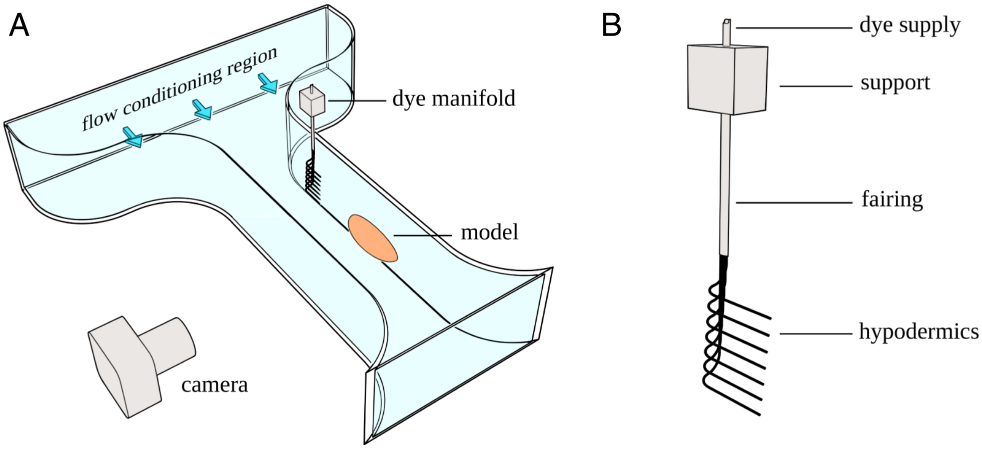

Fig. 8. Schematics of the experimental apparatus used for streakline visualizations. (*A*) Water tunnel test section, model, dye injection system, and camera. The particular arrangement shown here is relevant to overhead views such as that shown in Fig. 5*D*. (*B*) Zoomed-in view of the manifold used to produce dye streaklines.

the density of the dye solution, e.g. by adding alcohol, to that of water was not needed for the conditions studied here.

Numerical Methods. The numerical simulations are performed using a custom-written Matlab script, which is available on GitHub along with codes for plotting, visualization, and convergence analysis https://github.com/scott-weady/erosion.git (80). The code employs a second-order marker and cell finite difference discretization for the fluid velocity, with the phase-field located at cell centers on the staggered grid. The hydrodynamic and phase-field equations are integrated in time using a forward Euler discretization, coupled to a pressure projection method to enforce fluid incompressibility. The pressure Poisson equation is solved directly using a Cholesky decomposition coupled with a Fast Fourier Transform in the periodic y-direction. The computational domain measures $[0, 8] \times [0, 4] \times [0, 4]$ in dimensionless units and employs a grid of $300 \times 150 \times 150$, corresponding to a spacing $h \approx 0.0266$. The dimensionless regularization parameter is $m = 0.2\,h^2$, chosen to avoid stiffness associated with explicit time-stepping while also ensuring resolution of the diffusive length scale $\sqrt{m} \sim h$.

The phase-field model presents several numerical challenges to be overcome. First, the fact that $|\nabla\phi| \to 0$ away from the surface leads to ill conditioning of $\hat{\mathbf{n}}$ due to division by $|\nabla\phi|$. This is remedied by assuming a smoothed profile $\phi = [1 - \tanh(2n/\delta)]/2$ at the surface of the body (53), where n is the coordinate normal to the surface and $\delta = 2\,h$ is the interface thickness chosen to extend over several grid points. This yields $\kappa|\nabla\phi| = -(\nabla \cdot \hat{\mathbf{n}})|\nabla\phi| = \Delta\phi - \phi(1-\phi)(1-2\phi)/\delta^2$. The permeability coefficient η of Eq. **6** is chosen to be $\eta = 10\delta^2$, the scaling of which is chosen to match that of ref. 81 but with a smaller prefactor in order to better approximate the no-slip condition. We find that a time step of $\Delta t = 10^{-3} \ll \eta$ ensures numerical stability for all conditions studied here.

An additional challenge arises in evaluating the shear stress at the surface, which does not converge pointwise with the grid resolution for the phase-field model with volume penalization. Here, we make the approximation $|(\mathbf{I} - \hat{\mathbf{n}}\hat{\mathbf{n}}) \cdot \mathbf{\Sigma} \cdot \hat{\mathbf{n}}| \approx \alpha|\hat{\mathbf{n}} \times \mathbf{u}|/\mathrm{Re}\delta$, where $|\hat{\mathbf{n}} \times \mathbf{u}|$ is the magnitude of the tangential velocity and α is a constant. Because of how α appears in the erosion law (see below), its value need not be specified independently of the erodibility constant. To motivate the above approximation, consider the two-dimensional tangential velocity $u(s, n)$ of the true solution, where s is a tangential coordinate on the surface and n is the distance normal to the surface. Expanding about n gives $u(s, n) \approx u(s, 0) + n\partial u/\partial n|_{n=0} + O(n^2)$. Incorporating the no-slip condition $u(s, 0) = 0$ yields $u(s, n)/n \approx \partial u/\partial n|_{n=0} + O(n)$, to which the chosen approximation resembles a finite difference. For the choice of penalization parameters given in the previous paragraph, we find the volume-penalized solution $u_\delta(s, n)$ scales as $O(\delta)$, indicating that $u_\delta(s, n)/\delta$ approaches a finite value as $\delta \to 0$. Using the aforementioned approximations and the relation $\hat{\mathbf{n}} = -\nabla\phi/|\nabla\phi|$, the phase-field equation used in simulations then becomes $\partial\phi/\partial t = -\alpha C|\nabla\phi \times \mathbf{u}|/\mathrm{Re}\delta + m[\Delta\phi - \phi(1-\phi)(1-2\phi)/\delta^2]$. We therefore define $\tilde{C} = \alpha C/\mathrm{Re}$ as the effective erodibility constant whose value sets the timescale of the shape dynamics. Based on these approximations, the interface velocity as shown in Fig. 6 is computed from the formula $|v_n| = (\tilde{C}/\delta)|\nabla\phi \times \mathbf{u}|/|\nabla\phi| \approx -4\tilde{C}|\nabla\phi \times \mathbf{u}|$. The last approximation comes from the tanh form of the interface profile, which gives $|\nabla\phi||_{\phi=1/2} \approx [\phi(1-\phi)/\delta]|_{\phi=1/2} = 1/4\delta$ (53).

It is not clear that the approximation to the shear stress necessarily converges to the true value, and hence, the associated erosion law employed in the simulations is, strictly speaking, an alternative prescription for the boundary evolution. It is suggestive that the simulations reproduce shape dynamics broadly similar to those from experiments, and known boundary-layer theory scaling laws for the shear-induced removal rate are also recovered (e.g. Fig. 6*C*). We also note that similar issues with convergence arise in phase field models of melting, where Gibbs–Thomson-like laws serve as alternative models that converge to the Stefan condition (82).

Data, Materials, and Software Availability. Matlab script used in numerical simulations is available on Github (80). All other data are included in the manuscript and/or supporting information.

ACKNOWLEDGMENTS. We thank R. Mehta and K. Long of the NASA Ames Research Center for useful discussions on streakline visualization, and A. Kim and K. Li for assistance with the experiments. We also thank K. Überschär, K. Olmer, S. Oppo, E. Rovielo, M. Welland, J. Stephen, and I. B. Cabral for the photographs used in Fig. 1 and for providing scale estimates. We thank the two anonymous reviewers whose comments helped improve the manuscript. The simulations were performed thanks to both the Flatiron Institute's high-performance computing cluster and the New York University Greene supercomputer. L.R. acknowledges funding from the NSF through grants DMS-2206573 and DMS-1646339.

1. C. Cotton, *Climatic Accidents in Landscape Making* (Whitcombe and Tombs limited, 1942).
2. A. Ward, Yardangs on Mars: Evidence of recent wind erosion. *J. Geophys. Res.* **84**, 8147–8166 (1979).
3. A. Parsons, A. Abrahams, "Geomorphology of desert environments" in *Geomorphology of Desert Environments*, A. J. Parsons, A. D. Abrahams, Eds. (Springer, 1994), pp. 3–7.
4. H. Melosh, *Planetary Surface Processes* (Cambridge Univ. Press, 2011).
5. J. Perkins, N. Finnegan, S. de Silva, Amplification of bedrock canyon incision by wind. *Nat. Geosci.* **8**, 305–310 (2015).
6. M. Yalin, *Mechanics of Sediment Transport* (Pergamon, 1976).
7. R. Huggett, *Fundamentals of Geomorphology* (Taylor and Francis, 2011).
8. A. Goudie, Quantification of rock control in geomorphology. *Earth Sci. Rev.* **159**, 374–387 (2016).
9. A. Forte, B. Yanites, K. Whipple, Complexities of landscape evolution during incision through layered stratigraphy with contrasts in rock strength. *Earth Surf. Proc. Land.* **41**, 1736–1757 (2016).
10. M. Perne, M. Covington, E. Thaler, J. Myre, Steady state, erosional continuity, and the topography of landscapes developed in layered rocks. *Earth Surf. Dyn.* **5**, 85–100 (2017).
11. D. Peifer, C. Persano, M. Hurst, P. Bishop, D. Fabel, Growing topography due to contrasting rock types in a tectonically dead landscape. *Earth Surf. Dyn.* **9**, 167–181 (2021).
12. R. Grabowski, I. Droppo, G. Wharton, Erodibility of cohesive sediment: The importance of sediment properties. *Earth Sci. Rev.* **105**, 101–120 (2011).
13. H. Huppert, The intrusion of fluid mechanics into geology. *J. Fluid Mech.* **173**, 557–594 (1986).
14. L. Ristroph, M. N. J. Moore, S. Childress, M. Shelley, J. Zhang, Sculpting of an erodible body by flowing water. *Proc. Natl. Acad. Sci. U.S.A.* **109**, 19606–19609 (2012).
15. M. Moore, L. Ristroph, S. Childress, J. Zhang, M. Shelley, Self-similar evolution of a body eroding in a fluid flow. *Phys. Fluids* **25**, 116602 (2013).
16. M. N. J. Moore, Riemann-hilbert problems for the shapes formed by bodies dissolving, melting, and eroding in fluid flows. *Commun. Pure Appl. Math.* **70**, 1810–1831 (2017).
17. L. Ristroph, Sculpting with flow. *J. Fluid Mech.* **838**, 1–4 (2018).
18. P. Hersen, S. Douady, B. Andreotti, Relevant length scale of barchan dunes. *Phys. Rev. Lett.* **89**, 264301 (2002).
19. S. Courrech du Pont, Dune morphodynamics. *C. R. Phys.* **16**, 118–138 (2015).
20. J. Cardona Florez, E. de Moraes Franklin, The formation and migration of sand ripples in closed conduits: Experiments with turbulent water flows. *Exp. Therm. Fluid Sci.* **71**, 95–102 (2016).
21. D. Durian *et al*., What is in a pebble shape? *Phys. Rev. Lett.* **97**, 028001 (2006).
22. J. Bruthans *et al*., Sandstone landforms shaped by negative feedback between stress and erosion. *Nat. Geosci.* **7**, 597–601 (2014).
23. N. Taberlet, N. Plihon, Sublimation-driven morphogenesis of Zen stones on ice surfaces. *Proc. Natl. Acad. Sci. U.S.A.* **118**, e2109107118 (2021).
24. M. Wykes, J. Huang, G. Hajjar, L. Ristroph, Self-sculpting of a dissolvable body due to gravitational convection. *Phys. Rev. Fluids* **3**, 043801 (2018).
25. J. Huang, J. Tong, M. Shelley, L. Ristroph, Ultra-sharp pinnacles sculpted by natural convective dissolution. *Proc. Natl. Acad. Sci. U.S.A.* **117**, 23339–23344 (2020).
26. S. Weady, J. Tong, A. Zidovska, L. Ristroph, Anomalous convective flows carve pinnacles and scallops in melting ice. *Phys. Rev. Lett.* **128**, 044502 (2022).
27. J. Mac Huang, N. J. Moore, Morphological attractors in natural convective dissolution. *Phys. Rev. Lett.* **128**, 024501 (2022).
28. A. S. Goudie, Mega-Yardangs: A global analysis. *Geogr. Compass* **1**, 65–81 (2007).
29. E. Aguilera, I. Hernando, J. Rabassa, "Landscapes developed on ignimbrites" in *Advances in Geomorphology and Quaternary Studies in Argentina*, J. Rabassa, Ed. (Springer, 2017), pp. 1–46.
30. Z. Ding, J. Zhao, J. Wang, L. Zhongping, Yardangs on earth and implications to mars: A review. *Geomorphology* **364**, 107230 (2020).
31. J. Armstrong, C. Leovy, Long term wind erosion on Mars. *Icarus* **176**, 57–74 (2005).
32. T. Barchyn, Modeling the mechanisms behind Yardang evolution. *J. Geophys. Res. Earth Surf.* **123**, 618–621 (2018).
33. J. Pelletier *et al*., Controls on Yardang development and morphology: 1. Field observations and measurements at Ocotillo Wells, California. *J. Geophys. Res. Earth Surf.* **123**, 694–722 (2018).
34. J. Pelletier, Controls on Vardang development and morphology: 2. Numerical modeling. *J. Geophys. Res. Earth Surf.* **123**, 723–743 (2018).
35. P. Carling, Subaqueous "Yardangs": Analogs for aeolian Yardang evolution. *J. Geophys. Res. Earth Surf.* **118**, 276–287 (2011).
36. Z. T. Wang, H. T. Wang, Q. H. Niu, Z. B. Dong, T. Wang, Abrasion of Yardangs. *Phys. Rev. E* **84**, 031304 (2011).
37. J. Li *et al*., Yardangs in the Qaidam Basin, northwestern China: Distribution and morphology. *Aeolian Res.* **20**, 89–99 (2016).

38. Y. Lina, L. Xuc, G. Mub, Differential erosion and the formation of layered Yardangs in the Loulan region (Lop Nur), eastern Tarim Basin. *Aeolian Res.* **30**, 41–47 (2018).
39. D. Zhang *et al*., Landscape evolution and development of Eolian-modified unconsolidated gravel surfaces and Yardangs in the Hami Basin. *China. Geomorphol.* **368**, 107355 (2020).
40. M. Gutiérrez-Elorza, G. Desir, F. Gutiérrez-Santolalla, Yardangs in the semiarid central sector of the Ebro depression (NE Spain). *Geomorphology* **44**, 155–170 (2002).
41. M. Grolier, J. McCauley, C. S. Breed, N. Embabi, Yardangs of the western desert. *Geograph. J.* **146**, 86–87 (1980).
42. A. Ward, R. Greeley, Evolution of the Yardangs at Rogers Lake, California. *Geol. Soc. Am. Bull.* **95**, 829–837 (1984).
43. Z. Dong *et al*., Geomorphology and origin of Yardangs in the Kumtagh Desert, Northwest China. *Geomorphology* **139–140**, 145–154 (2012).
44. T. Barchyn, C. Hugenholtz, Yardang evolution from maturity to demise. *Geophys. Res. Lett.* **42**, 5865–5871 (2015).
45. Y. Wang *et al*., Formation and evolution of Yardangs activated by late Pleistocene tectonic movement in Dunhuang, Gansu Province of China. *J. Earth Syst. Sci.* **125**, 1603–1614 (2016).
46. R. S. Anderson, Erosion profiles due to particles entrained by wind: Application of an Eolian sediment-transport model. *Geol. Soc. Am. Bull.* **97**, 1270–1278 (1986).
47. J. Perkins, N. Finnegan, S. de Silva, M. Willis, Controls on Eolian landscape evolution in fractured bedrock. *Geophys. Res. Lett.* **46**, 12–20 (2019).
48. E. Blackwelder, Yardangs. *Bull. Geol. Soc. Am.* **45**, 159–166 (1934).
49. D. Tritton, *Physical Fluid Dynamics* (Springer, 1977).
50. Kg. H. Schlichting, *Boundary-Layer Theory* (Springer, 2016).
51. S. L. Wang *et al*., Thermodynamically-consistent phase-field models for solidification. *Phys. D Nonlinear Phenom.* **69**, 189–200 (1993).
52. D. M. Anderson, G. B. McFadden, A. A. Wheeler, Diffuse-interface methods in fluid mechanics. *Annu. Rev. Fluid Mech.* **30**, 139–165 (1998).
53. C. Beckermann, H. J. Diepers, I. Steinbach, A. Karma, X. Tong, Modeling melt convection in phase-field simulations of solidification. *J. Comput. Phys.* **154**, 468–496 (1999).
54. B. Favier, J. Purseed, L. Duchemin, Rayleigh-Bénard convection with a melting boundary. *J. Fluid Mech.* **858**, 437–473 (2019).
55. J. Purseed, B. Favier, L. Duchemin, E. W. Hester, Bistability in Rayleigh-Bénard convection with a melting boundary. *Phys. Rev. Fluids* **5**, 023501 (2020).
56. E. W. Hester, L. A. Couston, B. Favier, K. J. Burns, G. M. Vasil, Improved phase-field models of melting and dissolution in multi-component flows. *Proc. R. Soc. A* **476**, 20200508 (2020).
57. E. W. Hester, C. D. McConnochie, C. Cenedese, L. A. Couston, G. Vasil, Aspect ratio affects iceberg melting. *Phys. Rev. Fluids* **6**, 023802 (2021).
58. R. Yang, K. L. Chong, H. R. Liu, R. Verzicco, D. Lohse, Abrupt transition from slow to fast melting of ice. *Phys. Rev. Fluids* **7**, 083503 (2022).
59. R. Yang, C. J. Howland, H. R. Liu, R. Verzicco, D. Lohse, Morphology evolution of a melting solid layer above its melt heated from below. *J. Fluid Mech.* **956**, A23 (2023).
60. F. Golay, D. Lachouette, S. Bonelli, P. Seppecher, Interfacial erosion: A three-dimensional numerical model. *C. R. Méc.* **338**, 333–337 (2010).
61. F. Golay, D. Lachouette, S. Bonelli, P. Seppecher, Numerical modelling of interfacial soil erosion with viscous incompressible flows. *Comput. Methods Appl. Mech. Eng.* **200**, 383–391 (2011).
62. H. Muhlhaus, L. Gross, A. Scheuermann, Sand erosion as an internal boundary value problem. *Acta Geotech.* **10**, 333–342 (2015).
63. C. Henning, M. Brodbeck, C. Koch, S. Staudacher, T. Ricken, Phase-field model for erosion processes. *PAMM* **20**, e202000282 (2021).
64. P. Angot, C. H. Bruneau, P. Fabrie, A penalization method to take into account obstacles in incompressible viscous flows. *Numer. Math.* **81**, 497–520 (1999).
65. K. Amin, J. Huang, K. Hu, J. Zhang, L. Ristroph, The role of shape-dependent flight stability in the origin of oriented meteorites. *Proc. Natl. Acad. Sci. U.S.A.* **116**, 16180–16185 (2019).
66. S. Boury, S. Weady, L. Ristroph, Sculpting the sphinx. *Phys. Rev. Fluids* **8**, 110503 (2023).
67. H. Werlé, Hydrodynamic flow visualization. *Annu. Rev. Fluid Mech.* **5**, 361–386 (1973).
68. J. Huang, M. Moore, L. Ristroph, Shape dynamics and scaling laws for a body dissolving in fluid flow. *J. Fluid Mech.* **765**, R3 (2015).
69. A. Niedoroda, C. Dalton, A review of the fluid mechanics of ocean scour. *Ocean Eng.* **9**, 159–170 (1982).
70. F. Lachaussée, Y. Bertho, C. Morize, A. Sauret, P. Gondret, Competitive dynamics of two erosion patterns around a cylinder. *Phys. Rev. Fluids* **3**, 012302(R) (2018).
71. M. Zhao, A review on recent development of numerical modelling of local scour around hydraulic and marine structures. *J. Mar. Sci. Eng.* **10**, 1139 (2022).
72. S. de Silva, J. Bailey, K. Mandt, J. Viramonte, Yardangs in terrestrial ignimbrites: Synergistic remote and field observations on Earth with applications to Mars. *Planet. Space Sci.* **58**, 459–471 (2010).
73. F. El-Baz, C. Breed, M. Grolier, J. McCauley, Eolian features in the Western Desert of Egypt and some applications to Mars. *J. Geophys. Res.* **84**, 8205–8221 (1979).
74. F. El-Baz, Desert builders knew a good thing when they saw it. *Smithsonian* **12**, 116–121 (1981).
75. G. Gerster, F. El-Baz, Egypt's desert of promise. *Natl. Geogr.* **161**, 190–221 (1982).
76. K. Gauri, Geologic study of the Sphinx. *Newsl. Am. Res. Cent. Egypt* **127**, 24–43 (1984).
77. A. Duvall, E. Kirby, D. Burbank, Tectonic and lithologic controls on bedrock channel profiles and processes in coastal California. *J. Geophys. Res.* **109**, F03002 (2004).
78. J. Venditti *et al*., Flow in bedrock canyons. *Nature* **513**, 534–537 (2014).
79. C. Rennie, M. Church, J. Venditti, Rock control of river geometry: The Fraser canyons. *J. Geophys. Res. Earth Surf.* **123**, 1860–1878 (2018).
80. S. Boury, S. Weady, L. Ristroph, Data from "Yardangs sculpted by erosion of heterogeneous material." GitHub. https://github.com/scott-weady/erosion. Deposited 7 May 2024.
81. E. W. Hester, G. M. Vasil, K. J. Burns, Improving accuracy of volume penalised fluid-solid interactions. *J. Comput. Phys.* **430**, 110043 (2021).
82. G. Caginalp, Stefan and hele-shaw type models as asymptotic limits of the phase-field equations. *Phys. Rev. A* **39**, 5887–5896 (1989).